Ceramics International xxx (xxxx) xxx

Contents lists available at ScienceDirect

Ceramics International

journal homepage: www.elsevier.com/locate/ceramint

A comparative study of 5A and 13X zeolites doped by Eu^{3+} ion-exchange in water or ethanol

Anna Safonova [a,b], Nicola Daldosso [a], Michele Cassetta [a,c], Guilherme C. Concas [d], Tommaso Del Rosso [d], Akeem Akinwekomi [e], Farid Akhtar [e], Alberto Vomiero [e], Francesco Enrichi [a,f,*]

[a] Department of Engineering for Innovation Medicine, University of Verona, Strada le Grazie 15, 37134, Verona, Italy
[b] Department of Diagnostics and Public Health, University of Verona, Strada le Grazie 15, 37134, Verona, Italy
[c] Department of Earth Science, University of Torino, 10125 Torino, Italy
[d] Department of Physics, Pontifical Catholic University of Rio de Janeiro, Rua Marques de São Vicente 225, 22451-900, Rio de Janeiro, Brazil
[e] Department of Engineering Sciences and Mathematics, Luleå University of Technology, Luleå, 97187, Sweden
[f] CNR-ISP, Institute of Polar Sciences, Via Torino 155, 30172, Mestre-Venezia, Italy

ARTICLE INFO

Handling Editor: Dr P. Vincenzini

Keywords:
Zeolite
Europium
Ion exchange
Photoluminescence

ABSTRACT

Commercial zeolites are crystalline aluminosilicate materials with high surface area and porosity which can be used in several applications. This study aims at adding luminescent functionality to the zeolite network, either enabling optical monitoring of the capturing process or towards the development of efficient light-emitting materials. Two representative commercial zeolites were chosen: 5A and 13X, adding europium (Eu^{3+}) by an ion-exchange process. The effects of different solvents (water and ethanol) and thermal treatments on the structural and optical properties of the doped zeolites were investigated. The results demonstrate that 13X zeolites have superior Eu uptake and luminescent properties compared to 5A. XRD analysis suggests that Eu exchange can stress and disorder the network, which is recovered by annealing up to 600 °C. Instead, a higher temperature of 800 °C induces the collapsing of the porosity, with partial amorphization and significant reduction of the surface area of the material. The optical analysis showed that the PL intensities for 13X samples can be 60 times higher than those obtained for 5A samples. Moreover, ethanol emerged as a superior solvent to water, avoiding the presence of -OH vibrational energies detrimental to the luminescence of rare earth ions.

1. Introduction

Zeolites are crystalline porous materials widely used for environmental remediation, gas separation, and catalysis due to their structural properties and high surface area [1–9], but they can also be used as scaffold for luminescent species towards the development of phosphors for lighting [10–15]. These versatile properties make them interesting materials for multipurpose applications. Among zeolites, 13X and 5A present distinct geometries and porosities. Both are aluminosilicate molecular sieves, but the first has a faujasite-type structure (FAU), while the latter has a lynde-type A structure (LTA). Zeolite 13X is the sodium form of type X zeolite crystal structure. The effective pore opening is about 1.0 nm. The typical chemical formula is Na_{86} $[(AlO_2)_{86}(SiO_2)_{106}]$ · X H_2O, with a water content of about 21 % and PM of about 16,985 g/mol. Zeolite 5A is the calcium form of type A zeolite crystal structure. The effective pore opening is about 0.5 nm. The typical chemical formula is $Ca_{4.5}Na_3$ $[(AlO_2)_{12}(SiO_2)_{12}]$ · X H_2O, with a water content of about 21 % and PM of about 2124 g/mol.

Zeolites can be easily modified for obtaining specific properties. For example, rare earth ions (RE^{3+}) can be introduced in the structure by ion-exchange in solution, both in water and in ethanol solvents. Rare earth ions (RE^{3+}), such as Eu^{3+}, are especially intriguing due to their photoluminescent (PL) emissions, characterized by unique spectral features, long luminescence lifetimes, and transitions within the 4f energy levels [16].

Doping zeolites with luminescent activators can make them efficient phosphors for lighting or add sensing functionality to the material. In the latter application, while the porous structure can act as a sponge for the

This article is part of a special issue entitled: PRE'24 published in Ceramics International.

* Corresponding author. Department of Engineering for Innovation Medicine, University of Verona, Strada le Grazie 15, 37134, Verona, Italy.
E-mail address: francesco.enrichi@univr.it (F. Enrichi).

https://doi.org/10.1016/j.ceramint.2025.02.406
Received 15 October 2024; Received in revised form 14 January 2025; Accepted 28 February 2025
Available online 4 March 2025

capture of contaminants, the optical emission can be used to indicate the amount of contaminant and the eventual saturation of the trapping capability, requiring to be changed or renewed.

In the trivalent RE^{3+} ions, the optical transitions consist of weak magnetic dipole (MD) and induced electric dipole (ED) transitions. While the intensities of the MD transitions are not influenced by the chemical environment surrounding the ion, the ED transitions are very sensitive to it. Eu^{3+} is an ideal RE^{3+} model. Its red emission is widely used in phosphors for lighting and it can be easily detected. Unlike other RE^{3+} ions, Eu^{3+} luminescence, related to the $^5D_0 \rightarrow {}^7F_J$ transitions, is particularly sensitive to the local environment and can be used as a local probe [17–21] to get information on the site symmetry around it. In fact, the $^5D_0 \rightarrow {}^7F_2$ (about 610 nm) is a pure electric dipolar transition, while the $^5D_0 \rightarrow {}^7F_1$ (about 590 nm) is a pure magnetic dipolar transition. The higher the ratio between the intensity of these two transitions (Eq. (1)), the lower the local symmetry around Eu^{3+} is with respect to an inversion centre, since a high local symmetry strongly reduces the electric dipolar emission without affecting the magnetic dipolar one, and vice versa. Therefore, R is called the asymmetry ratio.

$$R = \frac{I(^5D_0 \longrightarrow {}^7F_2)}{I(^5D_0 \longrightarrow {}^7F_1)} \tag{1}$$

Another unique property related to the internal ^4f transitions of Eu^{3+} ions is that the intensity of the $^5D_0 \rightarrow {}^7F_1$ transition, being magnetic dipolar in character and therefore insensitive to change in the Eu^{3+} surroundings, may be taken as a reference, with a radiative rate of 50 s^{-1}. All the other observed transitions arising from the $^5D_0$ level have an electric dipolar character. Therefore, assuming the occurrence of only radiative and non-radiative processes in the depopulation of the $^5D_0$ excited level, from these two intensity ratios the $^5D_0$ radiative lifetime can be evaluated. From a practical point of view, the radiative lifetime (τ_{RAD}) can be calculated by the following equation:

$$\left(\frac{1}{\tau_{RAD}}\right)_{Eu} = 14.65\, n^3 \frac{I(^5D_0 \longrightarrow {}^7F_J)}{I(^5D_0 \longrightarrow {}^7F_1)}, \tag{2}$$

where n is the refractive index, $I(^5D_0 \rightarrow {}^7F_J)/I(^5D_0 \rightarrow {}^7F_1)$ is the ratio between the total integrated emission from the Eu $^5D_0$ level to the ^7F_J manifold ($J = 0$–6) and the integrated intensity of the transition $^5D_0 \rightarrow {}^7F_1$ [22,23].

Therefore, by comparing the experimental lifetime τ_{EXP} with the radiative lifetime calculated from the luminescence emission spectra τ_{RAD} it is possible to give an evaluation of the quantum efficiency QY of the emitting Eu^{3+} ions:

$$QY = \frac{\tau_{EXP}}{\tau_{RAD}} \tag{3}$$

A detailed description of these analysis was reported in a previous paper [24,37]. These features make Eu^{3+} a unique tool for the study and optimization of the system.

The investigation of Eu^{3+} co-doped 13X and 5A zeolites in different solvents, water and ethanol, can provide significant advances for the optimization of luminescent porous zeolites. Water is a standard solution for ion-exchange, but ethanol offers a better environment for RE^{3+} ions, which are sensitive to -OH groups that act as non-radiative recombination centers, reducing their optical efficiency. Post-exchange annealing treatments can be used to finely tune the material's crystallinity and the elemental arrangement, with the aim of maximizing photoluminescence without affecting porosity and capturing capabilities, for potential applications in environmental and energy technologies.

2. Experimental

In this study, commercial 5A and 13X zeolites were purchased from Luoyang Jianlong Micro-Nano New Materials Co., Ltd. The doping agent was Europium nitrate pentahydrate ($Eu(NO_3)_3 \cdot 5\, H_2O$) (Sigma Aldrich, USA), with concentrations meticulously chosen to ensure optimal doping efficiency.

The synthesis process began with the dissolution of europium nitrate in either water or ethanol to create a transparent doping solution, ensuring a final concentration of 0.0375 mol/L. Zeolite powders were then thoroughly mixed into these solutions, allowing for an hour-long ion exchange at room temperature. After exchange, the samples underwent centrifugation at 6500 rpm for 8 min, segregating the supernatant from the zeolite powder. The subsequent washing process involved two cycles, using the same solvent as in the dissolution step. The concentration of europium was increased fourfold for certain samples, and similar atomic content of silver was introduced for co-doping experiments. The powders were dried overnight at 70 °C, followed by a series of thermal treatments at 400 °C, 600 °C, and 800 °C in air to study the effects of temperature on the doped zeolites.

The samples were named accounting for the exchange solution and annealing temperature. As an example, EuXE400 refers to Eu-exchanged (Eu) 13X zeolite (X) exchanged in ethanol (E) and annealed at 400 °C (400), while EuAW refers to Eu-exchanged (Eu) 5A zeolite (A) in water (W) not annealed.

Characterization techniques included UV–Vis spectroscopy (Agilent Cary5000) to estimate the doping amount and Photoluminescence (PL) spectroscopy for emission analysis (Edinburgh Instruments FLS980). A continuous-wave xenon lamp or a microsecond-pulsed xenon flashlamp were used as excitation sources for steady-state or time-resolved measurements, respectively, selecting the excitation wavelength by a double-grating monochromator. The light emitted from the sample was collected by a single-grating monochromator and recorded by a photon counting R928P PMT cooled at −20 °C. Time-resolved PL decays were recorded in multi-channel-scaling (MCS) mode.

Scanning Electron Microscopy equipped with Energy-Dispersive X-ray Spectroscopy (SEM-EDX) (JEOL JSM-IT300 Scanning electron microscope) were utilized for morphological and elemental analysis. Prior to this, a Leica EMACE 200 was used to deposit a 10-nm platinum coating on the samples to minimize charging effects. The atomic composition was evaluated by averaging at least 10 points in different parts of each sample.

Crystal structures of the zeolites before and after ion-exchange and annealing was obtained by X-Ray Diffraction XRD (Empyrean PANalytical diffractometer) using a Cu Kα X-ray radiation at 40 kV and 45 mA.

Brunauer–Emmett–Teller (BET) surface area analysis provided insights into the porosity of the doped zeolites. The BET surface area of the samples was measured by nitrogen adsorption at −196 °C (Micromeritics Gemini VII 2390 surface area analyzer). All samples were degassed at 300 °C under high vacuum overnight prior to the adsorption measurements.

3. Results and discussion

Fig. 1 reports the UV–Vis absorption of the supernatant Eu-containing solution before and after exchange and washing with 13X and 5A zeolites. Both for water and for ethanol, it is shown that 13X zeolites have better Eu uptake compared to 5A. This is attested by the complete disappearance of Eu absorption peaks in the supernatant solution for 13X, while 5A still contains residual Eu, indicating that the larger pore size of 13X allows for better penetration and accommodation of Eu ions within the material. The calculated uptake is 100 % for 13X zeolites, but only 9 % and 16 % for 5A zeolites in ethanol and water respectively.

In Fig. 2 (left) a representative SEM image of the EuXE400 sample shows the typical granularity of the powders with regular shapes in the 1–2 μm range. All the samples were very similar on this scale, independently from the annealing temperature. In Fig. 2 (right) an example of EDX spectrum is reported, showing the characteristic elemental

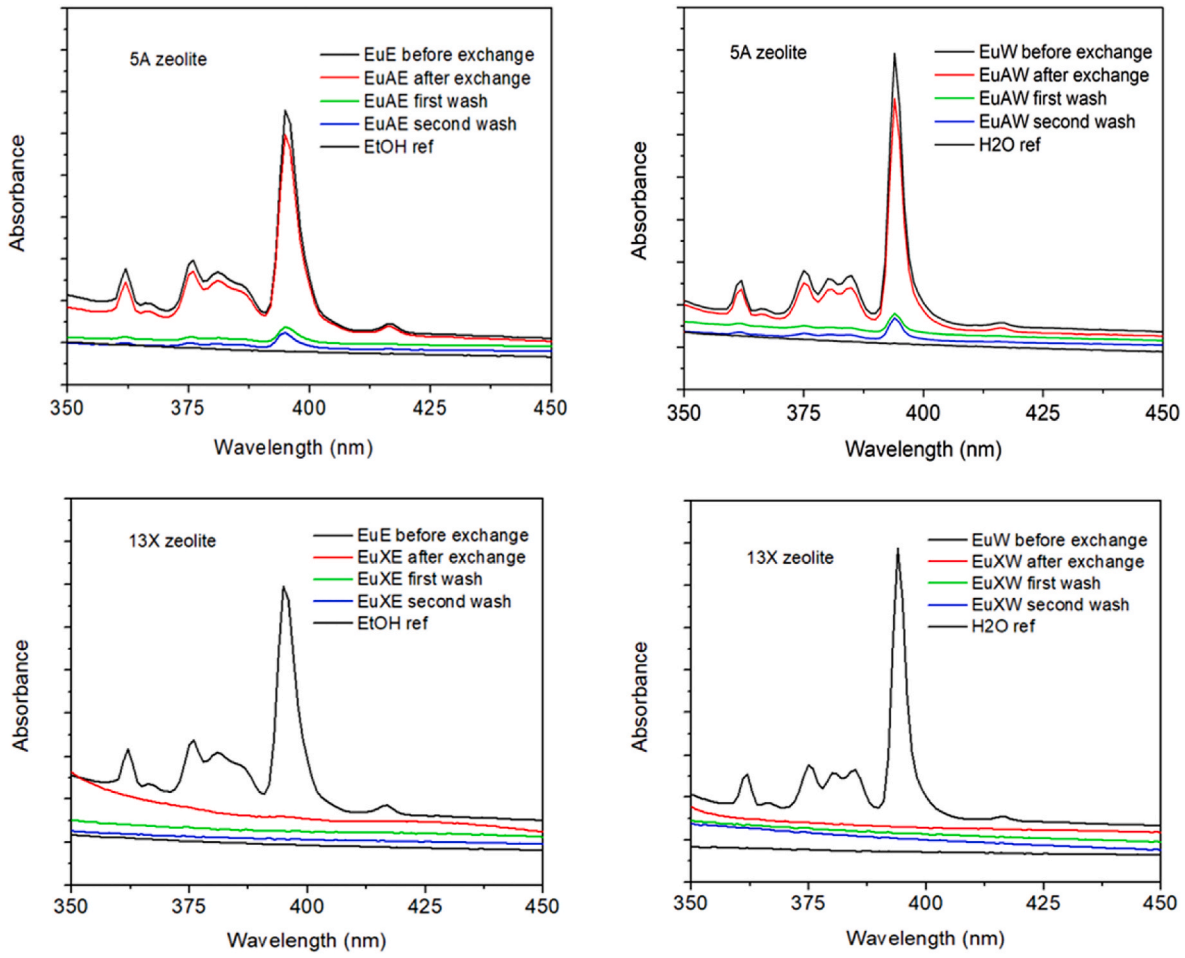

Fig. 1. UV–Vis absorption of Eu in the supernatant solution before exchange, after exchange and after washing in ethanol (E) and in water (W) for 5A (top) and 13X (bottom) zeolites.

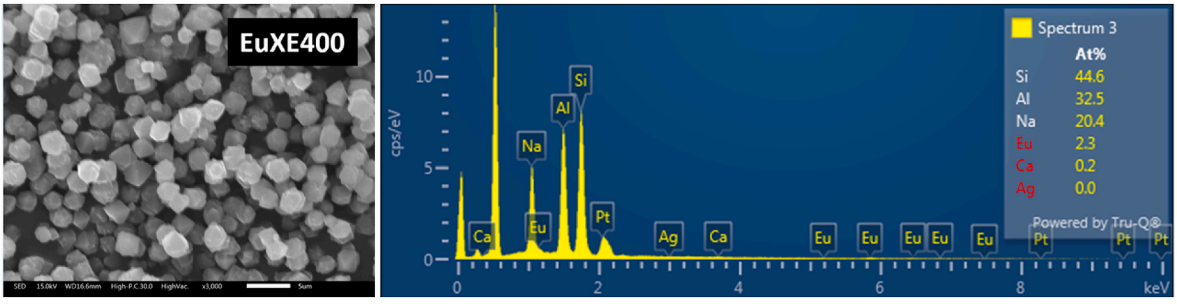

Fig. 2. (left) SEM images for EuXE400 samples, showing the typical granularity of the powder in the 1–2 μm size range; (right) example of EDX analysis of the same sample with the peaks related to the different elements and the calculation of the relative contributions.

peaks, with the calculation of the relative contribution.

The results of EDX analysis are reported in Table 1, revealing higher Eu concentrations in the 13X compared to the 5A zeolite. The amount of Eu after exchange, agrees with what was observed by UV–Vis absorption, showing a significant difference in the rare earth uptake for the 13X and the 5A zeolites. For the first, Eu values are in the 1.2–2.3 % range (relative concentration Eu/Si ≈ 3–5 %), while for the latter the concentration is 10 times lower, with a high uncertainty, close to the detection limit. It is worth noting that the solvent, ethanol or water, has a limited impact on Eu^{3+} exchange for both the zeolites, differently from other elements reported in the literature (Cu^{2+}, Cr^{3+}, Fe^{3+}) where it can play an important role in determining the final concentration of exchanged atoms due to the formation of different complexes in polar organic solvents with respect to water. [25]. Moreover, the elemental composition of the matrix before and after Eu exchange and annealing is not changed within the measurement uncertainty, and it is in agreement with the nominal elemental concentration.

Fig. 3 (left) reports XRD reflections on 13X zeolite before and after ion exchange and annealing up to 800 °C. It clearly shows the crystalline nature of the material, in agreement with the typical peaks tabulated for the faujasite-type structure (FAU) [26]. It is worth observing that the presence of crystalline Eu_2O_3 oxide or other Eu-based phases were not detected in Eu-exchanged samples, even for the highest annealing temperatures, suggesting the successful introduction of Eu ions in the

Table 1
Summary of EDX analysis of ion-exchanged zeolites, reporting the elemental composition of the samples. Oxygen was not selected in the elemental analysis.

Name	Elemental composition (at.%)				
	Al	Ca	Na	Si	Eu
Zeolite A	37.6	16.0	6.0	40.8	–
A-Eu-EtOH	37.8	16.0	5.4	40.6	<0.2
A-Eu-H_2O	38.1	15.2	4.8	41.8	<0.2
Zeolite X	32.7	–	22.0	45.0	–
X-Eu-EtOH	32.8	–	20.7	44.8	1.6
X-Eu-EtOH-400C	32.9	–	20.2	44.3	2.3
X-Eu-EtOH-600C	31.9	–	23.3	43.1	1.5
X-Eu-EtOH-800C	32.9	–	20.6	44.2	2.1
X-Eu-H_2O	34.1	–	17.3	46.6	1.7
X-Eu-H_2O-800C	32.8	–	21.0	44.6	1.2

zeolite crystalline network or they are highly dispersed on the zeolite surface.

The crystalline structure is almost unchanged up to 600 °C, but small modifications occur in the material treated at 800 °C, as shown for example in Fig. 3 (right). This was observed also in a previous study by Wu et al. [27], who related this behavior to the collapse of the zeolite structure, resulting in a more compact material with much decreased porosity. We will check this aspect later, by BET porosity analysis.

The X-ray diffraction (XRD) data in Fig. 3 were analyzed for the ethanol exchanged series. The crystallite size of the fabricated sample was determined by employing the Debye-Scherrer and the Williamson-Hall equation [28].

The Debye-Sherrer equation is the following:

$$D = \frac{K\lambda}{\beta \cos\theta} \tag{4}$$

where D is the average crystallite size, β is the Full Width at Half Maximum (FWHM) of the peak (in radians), θ is the diffraction angle, K is the Scherrer's factor (constant 0.98), λ is the X-ray wavelength.

Williamson-Hall (W-H) investigation has the advantage over the Debye-Scherrer's model that it allows the assessment of microstrain (ε) in addition to crystallite size (D) [29]. The W-H equation is defined as follows:

$$\beta \cos\theta = K\frac{\lambda}{D} + 4\varepsilon \sin\theta \tag{5}$$

where the additional parameter ε is the microstrain.

By plotting the FWHM component $\beta \cos\theta$ as a function of 4 sin θ we get the strain from the slope and the particle size from the y intercept. The samples were analyzed using the OriginLab software, with a fit performed for each sample and peak, thereby obtaining the structural parameters.

As an example, the analysis for the 800 °C annealed sample is reported in Fig. 4.

The results for the crystallinity percentage, crystallite size and microstrain are reported in Table 2. The crystallinity percentage is very similar for the different samples, with a slightly decreasing trend with increasing annealing temperature. Indeed, the thermally treated samples (EuXE400, EuXE600, and EuXE800) gradually decrease crystallinity, as confirmed by the vanishing of peaks at 22.7° (620), 27.7° (553), 29.6° (800), increasing the contribution of the amorphous phase. This can be explained in relation to the collapsing of the microporous structure of the zeolite, as anticipated earlier, which will be confirmed in the following of this paper.

The size of the crystallites determined using W–H plots are observed to be bigger than those determined by the D–S formula. The discrepancy in values is attributable to the effect of the strain component present in the synthesized nanocrystalline materials, which is not considered by the S-D equation. The untreated zeolite exhibits a value of 87 nm, whereas after exchange a significant increase in crystallite size is observed, of about 152 nm, followed by a reduction for higher annealing temperatures up to 600 °C. A significant difference is noted instead for the 800 °C annealing, which exhibits the maximum value of 179 nm. This overall behavior can be explained taking into account the microstrain (ε) parameter, which is representative of the structural evolution

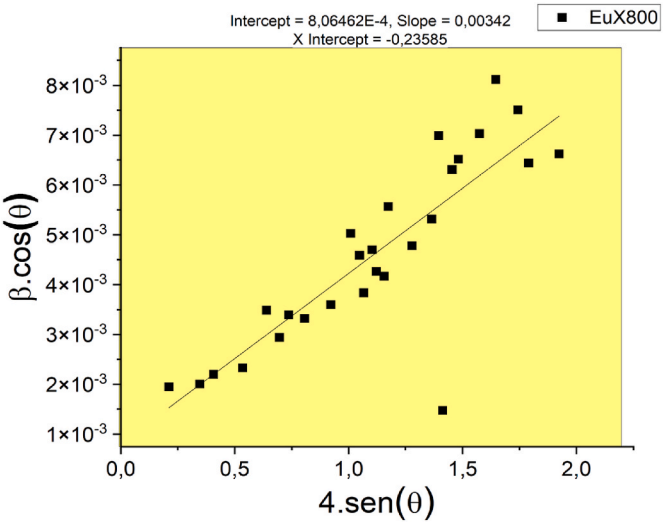

Fig. 4. W-H analysis for the 13X Eu-exchanged zeolite annealed at 800 °C.

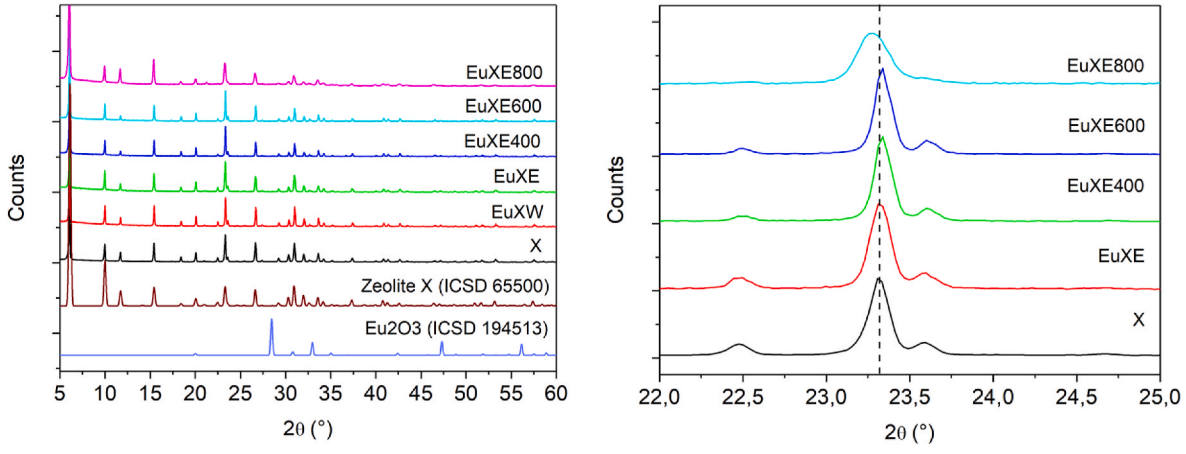

Fig. 3. XRD reflections for 13X zeolites before and after Eu exchange and annealed at different temperatures.

Table 2
XRD parameters (Crystallinity %, crystallite size and microstrain).

Sample	Crystallinity (%)	D-S Crystallite size (nm)	W-H Crystallite size (nm)	Microstrain (10^{-4})
EuXE800	80 ± 6	61	179	34.2
EuXE600	82 ± 4	85	105	3.8
EuXE400	87 ± 4	86	115	10.3
EuXE	86 ± 3	83	152	17.1
X	88 ± 3	80	87	8.4

of the system. The microstrain is indicative of the quality of the crystal. Higher values can be understood as a higher degree of deformation or more defects in the crystal. A low microstrain value of 8.4 $\cdot 10^{-4}$ is observed in the reference zeolite, while a significant increase occurs after ion exchange, indicating a significant internal stress and possible defectivity, which corroborates the introduction of Eu in the structure. Annealing at 400 °C and 600 °C releases stress and recover the structure, with an important reduction of the microstrain, reaching a value of 3.8 $\cdot 10^{-4}$ for the 600 °C annealing, lower than the one of the original zeolite structure. Finally, rising the annealing temperature to 800 °C results in an abrupt increase of the microstrain to 34.2 $\cdot 10^{-4}$ due to structural damage and collapsing of microporosity.

To better investigate this aspect, BET measurements were performed, with the aim of measuring the total surface area of the material. BET results are reported in Table 3.

It can be observed that similar values are reported for zeolite X and A, although they are characterized by different porosities in size and shape. In both cases, ethanol seems more effective in sample impregnation with respect to water, determining a stronger decrease in surface area for ethanol-exchanged zeolites with respect to water-exchanged ones. However, this is attributed to the retained solvent molecules after exchange, considering that the amount of dopants was found to be the same, as previously observed. Furthermore, a full recovery of the surface area is observed after 400 °C annealing, and higher values are reached for 600 °C annealing, due to the better and better release of trapped solvent molecules within the structure. A significant abrupt decrease of surface area is observed after 800 °C annealing, attesting the collapse of the pores, as anticipated in the discussion of the XRD analysis.

The different doping concentrations between 5A and 13X zeolites, as previously identified through UV–Visible spectroscopy and EDX measurements, have been confirmed by the intensity of PL emissions, shown in Fig. 5. PL values for 13X samples are 20–60 times higher than for 5A samples, with intensity variations related to annealing temperatures ranging from 2 to 3 times. The highest intensity is observed in 13X zeolite annealed at 400 °C. The PL emission spectrum also provides crucial insights into the Eu^{3+} ion environment. While the emission in 5A zeolites annealed at different temperatures is very similar, suggesting that europium is mostly outside the zeolite network, in 13X it shows different patterns for the different annealing temperatures, indicating different local ordering surrounding Eu^{3+}-ions which might be due to structural reorganization of the network and/or migration of Eu atoms with annealing at 400 °C and 600 °C, going to an increased disorder at 800 °C, indicated by peak broadening.

Table 3
BET surface area in different samples before and after ion-exchange and annealing.

Sample	BET surface area (m^2/g)
Zeolite X	436 ± 44
Zeolite A	497 ± 50
X-Eu-H_2O	534 ± 53
X-Eu-EtOH	378 ± 38
A-Eu-EtOH	284 ± 28
X-Eu-EtOH-400C	516 ± 52
X-Eu-EtOH-600C	600 ± 60
X-Eu-EtOH-800C	37 ± 4

The different asymmetry ratio R is reported in Table 4 for the various samples, with higher values related to lower centro-symmetric geometries. As a general comment, the precise control of the symmetry around Eu^{3+} ions, which can be obtained by specific complexing agents, for example, can result in ratios R that were reported from less than one to more than seventeen [30,31]. However, when Eu^{3+} ions are incorporated in solids, in particular in glassy materials, R-values are usually between three and four [32]. In crystalline materials they depend on the crystal symmetry and, above all, on the specific site occupied by the ions [33,34]. However, in the present case, there is little difference between A and X zeolites, which make difficult to attribute this value to a specific site. Indeed, we can conclude that the photoluminescence spectral shape is more indicative of the different crystal positions than the R-value.

Focusing on the 13X zeolite samples, the comparison between water and ethanol shows that ethanol emerges as a superior solvent, yielding PL intensity twice as high as water. It is known, in fact, that water vibrational energies are detrimental for the luminescence of rare earth ions, providing non-radiative recombination paths which compete with the radiative ones and finally reduce the quantum efficiency of the system, as reported in Table 5. This is not observed for 5A, further supporting the idea that Eu^{3+} ions are not able to enter the zeolite network. Indeed, the spectral shapes as well as the time-resolved luminescence decays, reported in Fig. 6, are very similar for the two solvents. In 13X the time-resolved PL analysis shows a single exponential decay for ethanol and a slightly non-exponential decay for water, suggesting non-radiative recombination centers in the latter. Additionally, lifetime values are generally longer for ethanol, with significantly higher quantum efficiency. Moreover, QY is as high as 80 % in the 800 °C annealed sample, and higher values could be obtained by further optimizing the annealing conditions. Indeed, values even higher, of almost 100 %, were reported in the literature [35,36]. Therefore, in applications where porosity is not needed, as for example in the lighting field, this material could have high potential.

Finally, it should be noted that time-resolved decays for 5A zeolites present a very steep initial drop, which is not an experimental artifact, but it is a real fast decay due to significant quenching processes, confirming the previous observations.

4. Conclusion

In this study we showed that Eu^{3+} can be easily introduced in commercial 13X and 5A zeolites by ion exchange in solution, providing luminescence properties to the materials. However, the doping of 13X zeolites is much more effective than the doping of 5A zeolites due to their larger pore size, which allows better ion accommodation and higher doping concentration.

Structural characterization revealed that Eu^{3+} can enter the crystalline network of 13X zeolites, resulting in some disorder and defects which can be recovered by annealing at 400 °C and 600 °C. Instead, further increase of the temperature to 800 °C has a detrimental effect, resulting in a collapse of the structure and a significant reduction of the surface area.

The optical analysis showed that the PL intensities for 13X samples can be 60 times higher than those obtained for 5A samples. Moreover, ethanol emerged as a superior solvent to water, avoiding the presence of -OH vibrational energies detrimental to the luminescence of rare earth ions.

These findings suggest that 13X zeolites Eu-exchanged in ethanol and annealed at 400 °C have promising applications in sensing and energy due to their enhanced luminescent properties, unchanged porosity and structural stability. Higher temperature annealing at 800 °C or above could instead be used as light emitting phosphors, reaching QY values as high as 80 %. Future research will focus on optimizing the doping process and exploring the applications in real-world scenarios.

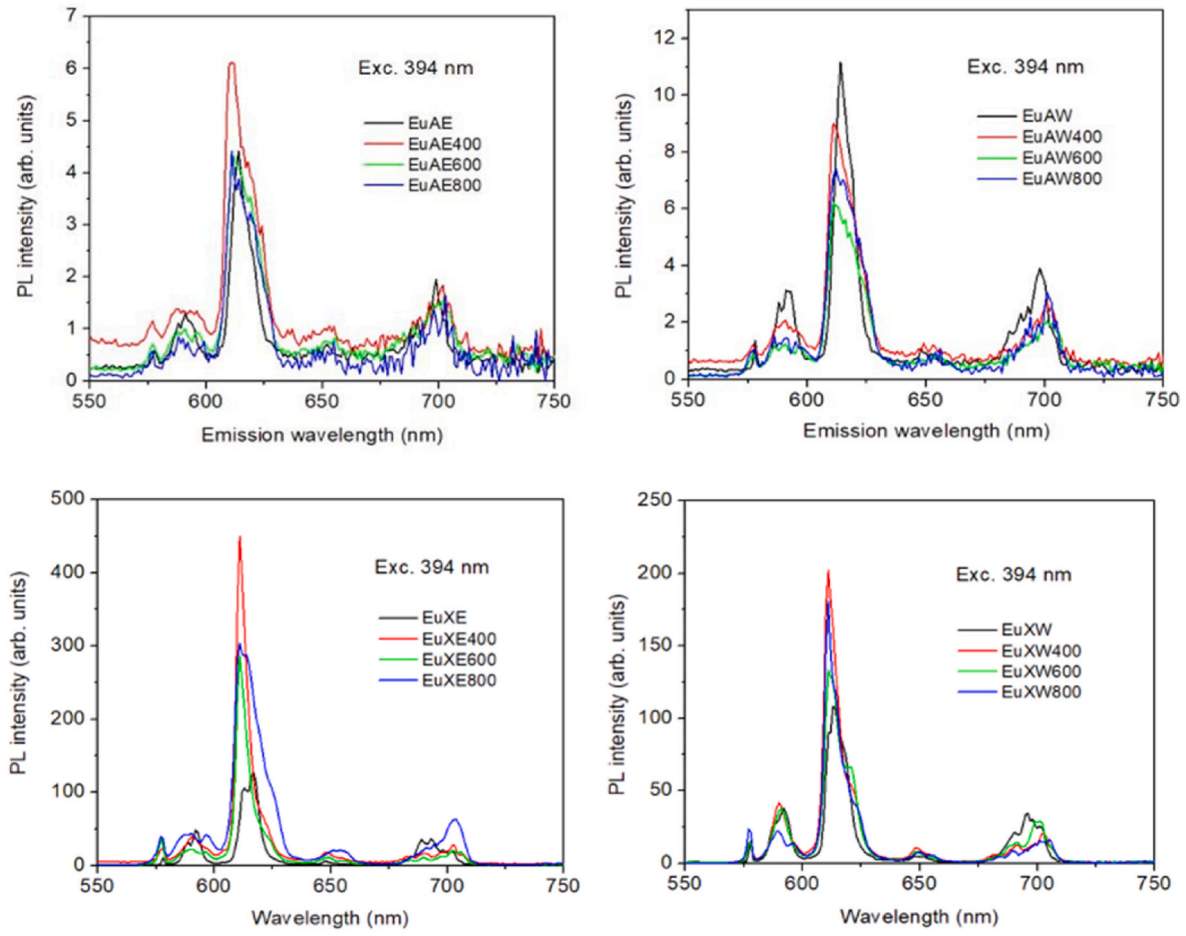

Fig. 5. Photoluminescence emission spectra, showing the typical Eu^{3+} transitions in the red spectral region, corresponding to the $^5D_0 \rightarrow {}^7F_J$ electronic transitions. Top row: A zeolite. Bottom row: X zeolite. Left: exchange in ethanol. Right: Exchange in water. (For interpretation of the references to colour in this figure legend, the reader is referred to the Web version of this article.)

Table 4
Site asymmetry ratio R of Eu^{3+} ions in the different samples. Reasonable uncertainty of these values is of the order of 5 %.

Name	Asymmetry ratio R
X-Eu-EtOH	3,4
X-Eu-EtOH-400C	6,2
X-Eu-EtOH-600C	6,6
X-Eu-EtOH-800C	5,6
X-Eu-H2O	3,4
X-Eu-H2O-400C	4,9
X-Eu-H2O-600C	4,4
X-Eu-H2O-800C	6,4
A-Eu-EtOH	3,3
A-Eu-EtOH-400C	4,6
A-Eu-EtOH-600C	4,3
A-Eu-EtOH-800C	5,5
A-Eu-H2O	3,7
A-Eu-H2O-400C	4,7
A-Eu-H2O-600C	6,3
A-Eu-H2O-800C	5,5

Table 5
Lifetime values for PL decay, radiative lifetimes and quantum efficiencies of Eu^{3+} emission in the different zeolite 13X samples. Reasonable uncertainty of these values is of the order of 5 %.

Name	Measured lifetime τ_{MEAS} (ms)	Radiative lifetime τ_{RAD} (ms)	Quantum efficiency QY (%)
X-Eu-EtOH	0,42	3,29	12,8
X-Eu-EtOH-400C	1,06	2,26	46,9
X-Eu-EtOH-600C	1,18	2,13	55,3
X-Eu-EtOH-800C	1,94	2,41	80,4
X-Eu-H2O	0,29	3,33	8,7
X-Eu-H2O-400C	0,63	2,81	22,4
X-Eu-H2O-600C	1,08	2,89	37,4
X-Eu-H2O-800C	1,22	2,22	54,9

CRediT authorship contribution statement

Anna Safonova: Writing – review & editing, Writing – original draft, Methodology, Investigation, Formal analysis, Data curation, Conceptualization. **Nicola Daldosso:** Writing – review & editing, Supervision, Resources, Methodology, Investigation. **Michele Cassetta:** Data curation, Formal analysis, Investigation, Writing – review & editing. **Guilherme C. Concas:** Data curation, Formal analysis, Investigation, Methodology, Writing – review & editing. **Tommaso Del Rosso:** Data curation, Formal analysis, Investigation, Methodology, Writing – review & editing. **Akeem Akinwekomi:** Methodology, Investigation, Formal analysis, Data curation. **Farid Akhtar:** Writing – review & editing,

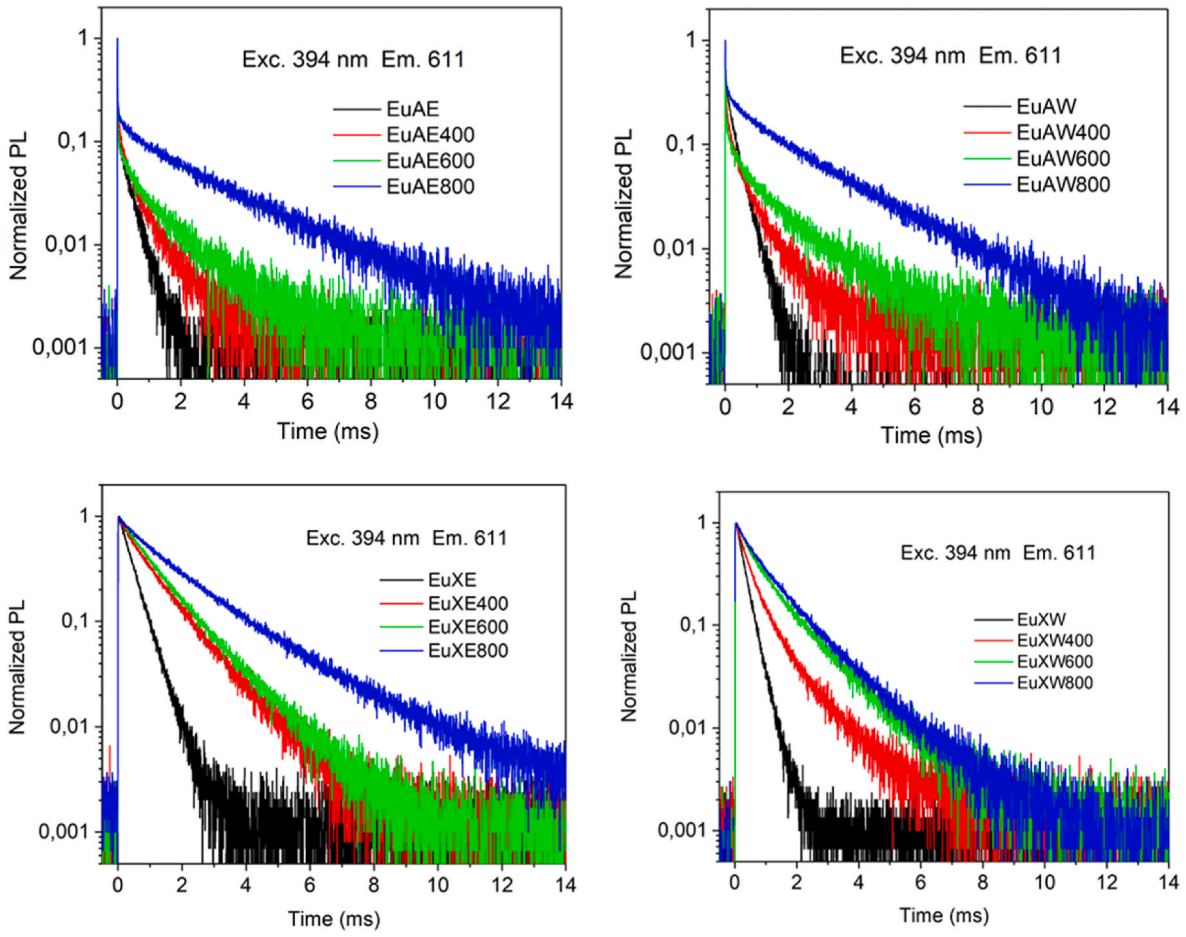

Fig. 6. Time resolved PL emission. Top row: 5A zeolite. Bottom row: 13X zeolite. Left: exchange in ethanol. Right: Exchange in water.

Supervision, Resources, Methodology, Investigation. **Alberto Vomiero:** Writing – review & editing, Validation, Supervision, Resources. **Francesco Enrichi:** Writing – review & editing, Writing – original draft, Validation, Supervision, Methodology, Investigation, Funding acquisition, Formal analysis, Data curation, Conceptualization.

Acknowledgements

The authors acknowledge Centro Piattaforme Tecnologiche (CPT) of the University of Verona for providing support with characterizations. F. E. would like to acknowledge the Short-Term Mobility program (STM) 2020 of CNR Italy, which funded the project "Eu and Ag doped zeolites for sensing and energy applications" and the project RIBA2022 of University of Verona entitled "SUNSHINE – SUstainable Nanoparticles Synthesis for HIgh performing eNergy and Environmental processes".

References

[1] N. Salahudeen, A review on zeolite: application, synthesis and effect of synthesis parameters on product properties, Chem. Africa 5 (6) (2022) 1889–1906, https://doi.org/10.1007/S42250-022-00471-9.

[2] S. Kumar, R. Srivastava, J. Koh, Utilization of zeolites as CO2 capturing agents: advances and future perspectives, J. CO2 Util. 41 (2020) 101251, https://doi.org/10.1016/J.JCOU.2020.101251.

[3] M. Hong, L. Yu, Y. Wang, J. Zhang, Z. Chen, L. Dong, Q. Zan, R. Li, Heavy metal adsorption with zeolites: the role of hierarchical pore architecture, Chem. Eng. J. 359 (2019) 363–372, https://doi.org/10.1016/J.CEJ.2018.11.087.

[4] L. Velarde, M.S. Nabavi, E. Escalera, M.L. Antti, F. Akhtar, Adsorption of heavy metals on natural zeolites: a review, Chemosphere 328 (2023) 138508, https://doi.org/10.1016/J.CHEMOSPHERE.2023.138508.

[5] F. Akhtar, Q. Liu, N. Hedin, L. Bergström, Strong and binder free structured zeolite sorbents with very high CO2-over-N2 selectivities and high capacities to adsorb CO2 rapidly, Energy Environ. Sci. 5 (2012) 7664–7673, https://doi.org/10.1039/C2EE21153J.

[6] Z. Cao, X. Cai, A.C. Feltrin, P. Feng, A. Kaiser, F. Akhtar, Calcium/strontium chloride impregnated zeolite A and X granules as optimized ammonia sorbents, RSC Adv. 12 (2022) 35115–35122, https://doi.org/10.1039/D2RA02981B.

[7] L. Velarde, M.S. Nabavi, E. Escalera, M.L. Antti, F. Akhtar, Adsorption of heavy metals on natural zeolites: a review, Chemosphere 328 (2023) 138508, https://doi.org/10.1016/J.CHEMOSPHERE.2023.138508.

[8] M. Delkash, B. Ebrazi Bakhshayesh, H. Kazemian, Using zeolitic adsorbents to cleanup special wastewater streams: a review, Microporous Mesoporous Mater. 214 (2015) 224–241, https://doi.org/10.1016/J.MICROMESO.2015.04.039.

[9] E. Pérez-Botella, S. Valencia, F. Rey, Zeolites in adsorption processes: state of the art and future prospects, Chem. Rev. 122 (2022) 17647–17695, https://doi.org/10.1021/acs.chemrev.2c00140.

[10] H. Wu, X. Yang, X. Yu, J. Liu, H. Yang, H. Lv, K. Yin, Preparation and optical properties of Eu3+/Eu2+ in phosphors based on exchanging Eu3+-zeolite 13X, J. Alloys Compd. 480 (2009) 867–869, https://doi.org/10.1016/J.JALLCOM.2009.02.050.

[11] M. Aoyama, T. Hayakawa, S. Honda, Y. Iwamoto, Development of zeolite-derived novel aluminosilicate phosphors, J. Lumin. 132 (2012) 2603–2607, https://doi.org/10.1016/J.JLUMIN.2012.05.014.

[12] K. Kennes, E. Coutino-Gonzalez, C. Martin, W. Baekelant, M.B.J. Roeffaers, M. Van der Auweraer, Silver zeolite composites-based LEDs: a novel solid-state lighting approach, Adv. Funct. Mater. 27 (2017) 1606411, https://doi.org/10.1002/ADFM.201606411.

[13] Y. Wang, H. Li, Luminescent materials of zeolite functionalized with lanthanides, CrystEngComm 16 (2014) 9764–9778, https://doi.org/10.1039/C4CE01455C.

[14] X. Zhou, T. Ren, J. Yin, X. Zhang, P. Li, H. Li, A full visible LED enabled by a broadband yellow emission nepheline phosphor derived from a europium doped SOD zeolite, J. Mater. Chem. C 10 (2022) 15613, https://doi.org/10.1039/d2tc02732a.

[15] W. Chen, R. Sammynaiken, Y. Huang, Photoluminescence and photostimulated luminescence of Tb3+ and Eu3+ in zeolite-Y, J. Appl. Phys. 88 (2000) 1424–1431, https://doi.org/10.1063/1.373834.

[16] G. Liu, B. Jacquier (Eds.), Spectroscopic Properties of Rare Earths in Optical Materials, Springer-Verlag Berlin Heidelberg, Germany, 2006, https://doi.org/10.1007/3-540-28209-2.

[17] D. Levy, R. Reisfeld, D. Avnir, Fluorescence of europium(III) trapped in silica gel-glass as a probe for cation binding and for changes in cage symmetry during gel dehydration, Chem. Phys. Lett. 109 (1984) 593–597, https://doi.org/10.1016/0009-2614(84)85431-7.

[18] S.K. Gupta, B. Rajeshwari, S.N. Achary, S.J. Patwe, A.K. Tyagi, V. Natarajan, R. M. Kadam, Europium luminescence as a structural probe: structure-dependent changes in Eu3+-substituted Th(C2O4)2·xH2O (x = 6, 2, and 0), Eur. J. Inorg. Chem. 2015 (2015) 4429–4436, https://doi.org/10.1002/ejic.201500623.

[19] D. V Deyneko, I. V Nikiforov, D.A. Spassky, Y.Yu Dikhtyar, S.M. Aksenov, S. Yu Stefanovich, B.I. Lazoryak, Luminescence of Eu3+ as a probe for the determination of the local site symmetry in β-Ca3(PO4)2-related structures, CrystEngComm 21 (2019) 5235–5242, https://doi.org/10.1039/C9CE00931K.

[20] R. Reisfeld, E. Zigansky, M. Gaft, Europium probe for estimation of site symmetry in glass films, glasses and crystals, Mol. Phys. 102 (2004) 1319–1330, https://doi.org/10.1080/00268970410001728609.

[21] R. Marin, G. Sponchia, E. Zucchetta, P. Riello, F. Enrichi, G. De Portu, A. Benedetti, Monitoring the t → m martensitic phase transformation by photoluminescence emission in Eu3+-doped zirconia powders, J. Am. Ceram. Soc. 96 (2013) 2628–2635, https://doi.org/10.1111/jace.12363.

[22] C. Malba, U.P. Sudhakaran, S. Borsacchi, M. Geppi, F. Enrichi, M.M. Natile, L. Armelao, T. Finotto, R. Marin, P. Riello, A. Benedetti, Structural and photophysical properties of rare-earth complexes encapsulated into surface modified mesoporous silica nanoparticles, Dalton Trans. 43 (2014) 16183–16196, https://doi.org/10.1039/c4dt00760c.

[23] M.H.V. Werts, R.T.F. Jukes, J.W. Verhoeven, The emission spectrum and the radiative lifetime of Eu3+ in luminescent lanthanide complexes, Phys. Chem. Chem. Phys. 4 (2002) 1542–1548, https://doi.org/10.1039/b107770h.

[24] F. Enrichi, G. Mastantuoni, M. Cassetta, A. Sambugaro, N. Daldosso, A. Martucci, A. Vomiero, E. Cattaruzza, G.C. Righini, Structural and optical properties of Eu3+-doped sol–gel silica–soda glasses, Europ. Phys. J. Plus 139 (2024) 346, https://doi.org/10.1140/EPJP/S13360-024-05151-W.

[25] V.J. Inglezakis, M.D. Loizidou, Ion exchange of some heavy metal ions from polar organicsolvents into zeolite, Desalination 211 (2007) 238–248, https://doi.org/10.1016/J.DESAL.2006.02.094.

[26] M.M.J. Treacy, J.B. Higgins, Collection of Simulated XRD Powder Patterns for Zeolites, fifth ed., 2007, https://doi.org/10.1016/B978-0-444-53067-7.X5470-7.

[27] H. Wu, X. Yang, X. Yu, J. Liu, H. Yang, H. Lv, K. Yin, Preparation and optical properties of Eu3+/Eu2+ in phosphors based on exchanging Eu3+-zeolite 13X, J. Alloys Compd. 480 (2009) 867–869, https://doi.org/10.1016/J.JALLCOM.2009.02.050.

[28] P. Kumar, D. Singh, I. Gupta, S. Singh, S. Nehra, R. Kumar, Realization of warm reddish-orange light emitter single phase Y4Al2O9:Sm3+ nanophosphors for indoor lighting applications, J. Lumin. 257 (2023) 119703, https://doi.org/10.1016/J.JLUMIN.2023.119703.

[29] P. Kumar, D. Singh, I. Gupta, UV excitable GdSr2AlO5:Eu3+ red emitting nanophosphors: structure refinement, photoluminescence, Judd-Ofelt analysis and thermal stability for w-LEDs, J. Alloys Compd. 966 (2023) 171410, https://doi.org/10.1016/J.JALLCOM.2023.171410.

[30] R. Zairov, A. Dovzhenko, N. Terekhova, T. Kornev, Y. Zhou, Z. Huang, D. Tatarinov, G. Nizameeva, R.R. Fayzullin, A.T. Gubaidullin, T. Salikhova, F. Enrichi, V.F. Mironov, A. Mustafina, Phosphineoxide-chelated europium(III) nanoparticles for ceftriaxone detection, Nanomaterials 13 (2023) 438, https://doi.org/10.3390/NANO13030438/S1.

[31] R.R. Zairov, A.P. Dovzhenko, S.N. Podyachev, S.N. Sudakova, T.A. Kornev, A. E. Shvedova, A.N. Masliy, V.V. Syakaev, I.S. Alekseev, I.M. Vatsouro, G. S. Mambetova, D.V. Lapaev, I.R. Nizameev, F. Enrichi, A.M. Kuznetsov, V. V. Kovalev, A.R. Mustafina, Role of PSS-based assemblies in stabilization of Eu and Sm luminescent complexes and their thermoresponsive luminescence, Colloids Surf. B Biointerfaces 217 (2022) 112664, https://doi.org/10.1016/J.COLSURFB.2022.112664.

[32] F. Enrichi, G. Mastantuoni, M. Cassetta, A. Sambugaro, N. Daldosso, A. Martucci, A. Vomiero, E. Cattaruzza, G.C. Righini, Structural and optical properties of Eu3+-doped sol–gel silica–soda glasses, Europ. Phys. J. Plus 139 (4) (2024) 1–10, https://doi.org/10.1140/EPJP/S13360-024-05151-W.

[33] V.A. Pustovarov, A.A. Vasin, M.G. Zuev, Site-selective luminescence of Eu3+ ions in silicate-tungstates with apatite and scheelite structures, Opt. Mater. X 15 (2022) 100186, https://doi.org/10.1016/J.OMX.2022.100186.

[34] M. Kowalczyk, T.F. Ramazanova, V.D. Grigoryeva, V.N. Shlegel, M. Kaczkan, B. Fetliński, M. Malinowski, Optical investigation of Eu3+ doped Bi12GeO20 (BGO) crystals, Crystals 10 (2020) 285, https://doi.org/10.3390/CRYST10040285.

[35] B. Bondzior, C. Nguyen, T.H. Quan Vu, D. Pugliese, P.J. Dereń, L. Petit, The usability of the Judd-Ofelt theory for luminescent thermometry using Eu3+-doped phosphate glass, J. Lumin. 252 (2022) 119386, https://doi.org/10.1016/J.JLUMIN.2022.119386.

[36] R. Schmechel, M. Kennedy, H. Von Seggern, H. Winkler, M. Kolbe, R.A. Fischer, X. Li, A. Benker, M. Winterer, H. Hahn, Luminescence properties of nanocrystalline Y2O3:Eu3+ in different host materials, J. Appl. Phys. 89 (2001) 1679–1686, https://doi.org/10.1063/1.1333033.

[37] F. Enrichi, M. Cassetta, N. Daldosso, E. Cattaruzza, P. Riello, R. Zairov, A. Vomiero, G.C. Righini, Effect of the crystal structure on the optical properties and Ag sensitization of Tb^{3+}/Yb^{3+} ions in silica-zirconia glasses and glass-ceramics, Ceram. Int. (2022). https://doi.org/10.1016/j.ceramint.2022.10.036.